Research Article Vol. 13, No. 11 / 1 Nov 2023 / *Optical Materials Express* 3394

Optical Materials EXPRESS

Light scattering features induced by residual layers in dielectric dewetted nanoparticles

NICOLETTA GRANCHI,[1,7] LUCA FAGIANI,[2,3] CHIARA BARRI,[2,3] ALEXEY FEDOROV,[3] MARCO ABBARCHI,[4,5] MARIA ANTONIETTA VINCENTI,[6] FRANCESCA INTONTI,[1] AND MONICA BOLLANI[3,8]

[1] *LENS and Department of Physics and Astronomy, University of Florence, Sesto Fiorentino, Italy*
[2] *Department of Physics, Politecnico di Milano, Milan, Italy*
[3] *Institute of Photonic and Nanotechnology - Consiglio Nazionale delle Ricerche, LNESS Laboratory, Como, Italy*
[4] *Aix Marseille Univ, Université de Toulon, CNRS, IM2NP Marseille, France*
[5] *Solnil, 95 Rue de la République, Marseille, 13002, France*
[6] *Department of Information Engineering, University of Brescia, Brescia, Italy*
[7] *granchi@lens.unifi.it*
[8] *monica.bollani@ifn.cnr.it*

Abstract: All-dielectric, sub-micrometric particles obtained through solid state dewetting of thin SiGe-films have been shown to support Mie resonances together with a high-quality monocrystalline composition and atomically smooth facets. Recently, a precise study on the impact given by the effective complex morphology of a SiGe dewetted nanoparticle to the Mie scattering properties has been provided and carried on through a novel experimental technique called Dark-field Scanning Optical Microscopy. In this work, by means of the same experimental technique and numerical simulations of light scattering, we show how the presence of a pedestal enriched with silicon placed under the SiGe-nanoparticle results in a sharp peak at high energy in the total scattering cross-section. Exploiting a tilted illumination to redirect scattered light, we are able to discriminate the spatial localization of the pedestal-induced resonance. Our results contribute to extending the practical implementations of dewetted Mie resonators in the field of light scattering directionality, sensing applications and show further engineering options beyond the simple isolated-island case.

1. Introduction

Sub-wavelength optical resonators enable efficient manipulation of electromagnetic fields at the nanoscale thanks to their directional scattering patterns and can be used as building blocks for functional metasurfaces [1–5]. All-dielectric nanoparticles can support multiple Mie resonances from electric and magnetic modes of different order. Their unidirectional scattering behavior, which is similar to classical antennas, results from constructive and destructive interference between electric and magnetic modes within the volume of the nanoparticles [6–11]. High scattering directivity in combination with a high degree of flexibility for light direction is desirable for the effective operation of many practical optical devices for nanocircuitry and sensing, and for this reason their optical properties have been widely studied and characterized [11,12–14]. In this work we analyze the scattering properties of residual layers in dielectric monocrystalline, atomically smooth nanoantennas realized via solid- state dewetting. This method that exploits the natural instability of thin films to form a variety of nanostructures with high fidelity over hundreds of repetitions and extremely large scales [15–18], has emerged among several alternatives as one of the most convenient approaches thanks to its scalability and the possibility to form ordered and disordered structures via self-assembly [18–20]. The optical properties of self-assembled nanostructures have been widely investigated in many previous works, both in the near-field [21]

#498142 https://doi.org/10.1364/OME.498142
Journal © 2023 Received 16 Jun 2023; revised 21 Jul 2023; accepted 21 Jul 2023; published 1 Nov 2023

and in the far-field [22,23], highlighting how Mie resonances sustained by the nanoantennas under tilted illumination, can generate radiation patterns in different directions [24]. Here, we analyse through light scattering simulations and by means of the Scanning Dark-field Optical Microscopy (SDOM) how an extra radiation lobe is generated by the scattering of the pedestal where the dewetted island is sitting on. In fact, the actual chemical composition of this residual layer has never been rigorously studied. Although the fabrication process suggests that one should consider a pedestal made of pure SiO_2, we consider that some intermixing phenomena take place during the annealing treatments, favoring a partial diffusion of silicon atoms in the silica film [25,26] . A selective wet etching process is here optimized, confirming the final chemical composition of the dewetted system after annealing treatments. As a result, the pedestal composition is not a pure SiO_2 thermal material of the original BOX, but a film enriched in silicon which we refer to as SiOx, characterized by peculiar optical properties.

2. Methods

2.1. Sample fabrication

Our samples consist in $Si_{0.7}Ge_{0.3}$ arrays of islands obtained through a hybrid top-down/bottom-up approach by means of templated solid state dewetting. The initial thickness of the top $Si_{0.7}Ge_{0.3}$ film is 26 nm, deposited over a monocrystalline, (001)-oriented, silicon on insulator (SOI) wafer with a device thickness of 7 nm and a buried SiO_2 layer of 25 nm. Squared $Si_{0.7}Ge_{0.3}$ patches are fabricated by means of electron beam lithography (EBL), reactive ion etching (RIE) (Fig. 1(a)). A cleaning step before the annealing process is carried out using acetone and diluted fluoridric acid (DHF, at 2% in vol). Upon annealing, they undergo a solid-state dewetting process forming self-assembled monocrystalline faceted islands, directly formed on the 25 nm layer of SiO_2 [15,21,27]. As rigorously demonstrated through phase-field simulations in [24], the resulting resonators (Fig. 1(b)) exhibit clear faceting on their surface conducible to [001], [111] and [113] crystalline planes as confirmed also by the 3D island (Fig. 1(c)) and profile (Fig. 1(d)) reconstructed via atomic force microscopy (AFM). These are the typical facets with which islands of Ge or SiGe are formed with bottom up processes [28,29].

In this work, we focus on the presence of the squared pedestal that is clearly visible in the inset of the SEM image of Fig. 1(b). The dry etching process, aimed at realizing the square pattern in silicon film before the annealing processes, cannot be exactly tuned and a slight etching in the SiO_2 layer is always achieved [15,17]. Specifically, the pattern is transferred to the thin Si film by reactive ion etching (RIE), using a CF_4 plasma, 50 WRF power and a total gas pressure of 5.4 mTorr for 30 sec. Decreasing the etching time by a few seconds, it is not guaranteed to arrive at the interface between silicon and silica, nullifying the possibility of controlling the dewetting processes. The pedestal, which is a result of such nanofabrication process as reported in Ref. [17], sustains every dewetted island and has a thickness of $\approx$ 12-14 nm as suggested from AFM measurements.

2.2. FDTD simulations

Light scattering simulations are performed by means of the finite difference time domain (FDTD) commercial softwares Lumerical [30]. In the simulations, the resonator is modelled accordingly with the structural parameters found in Ref. [24], i.e., a vertical aspect ratio of 0.6 and cupola shape. . We employ a Total Field Scattered Field (TFSF) source, which launches a broad-band (λ=300-900 nm) plane wave from the top and filters out all the light that has not been scattered. The TFSF source can be tilted with respect to the vertical axis. Power transmission monitors are positioned around the TFSF source to obtain the total scattering cross section. Optical constants for Si and SiGe are taken respectively from Aspnes [31], Jellison [32] and Malitson [33].

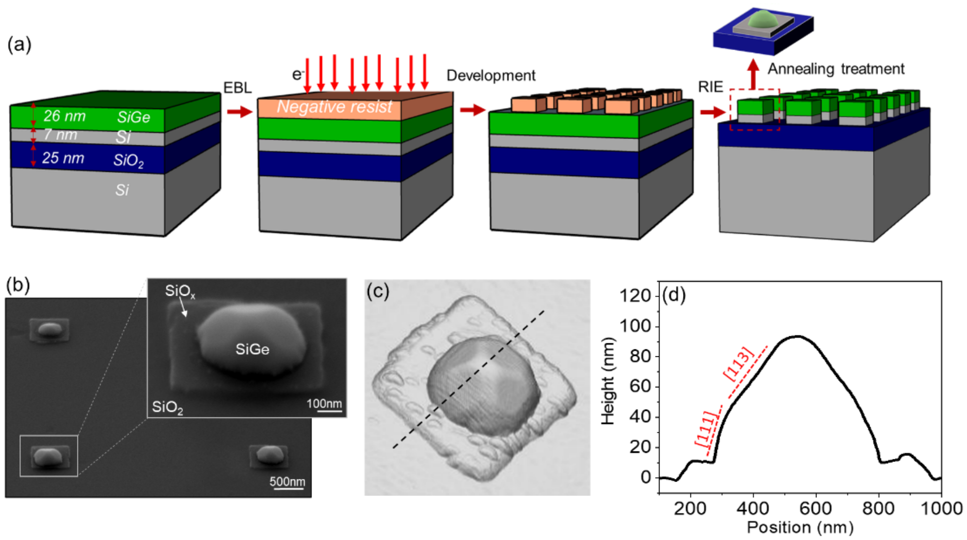

Fig. 1. a) Schematic sequence of the fabrication steps to realize ordered dielectric dewetted nanoparticles: the 26 nm of $Si_{0.7}Ge_{0.3}$ film is deposited over SOI wafer, and, after the spin coating of AR-N 7520.07 negative resist, the surface is exposure by EBL [27]. The exposed areas are developed by tetramethylammonium hydroxide and the SiGe/Si layer is etched by RIE. A cleaning step before the annealing process is carried out using acetone and diluted fluoridric acid. b) SEM characterization of SiGe resonator with crystalline facets formed on SiO_x pedestal film. c) 3D reconstructed AFM image of a single crystalline dewetted island. d) AFM profile of the island obtained by the transversal section on c) highlighted with the black dashed line.

2.3. *SDOM experiment*

The SDOM experiment is carried out by using a custom-built setup in which the dark-field condition is achieved by illuminating the islands with a light source tilted by an angle of 30°, larger than the collection angle of the objective lens (NA = 0.45), with respect to the axis normal to the substrate. The illumination source is a supercontinuum laser, and the illumination spot has a diameter of approximately 20 µm. The objective lens collects the scattered light, that is then fed into a multimode optical fiber of 10 µm diameter (that acts as a spatial filter) before being dispersed by a monochromator and detected with a Si-based CCD camera [24]. The overall collection spot has a diameter of ≈ 1 µm. The sample is mounted on a xy piezoelectric stage that allows to obtain dark-field spatially-resolved maps, collecting a single scattering spectrum for every position of the nanoantenna. It has been shown that this technique can provide dark-field spectra of single resonators, and hyperspectral maps that allow to spectrally isolate the Mie resonances contribution to the total scattering cross-section [24].

3. Results and discussion

We focus our attention on two dewetted islands of different sizes: one with radius R = 50 nm and one with R = 80 nm. The upper graphs of Fig. 2(a) and 2(b) show the experimental scattering spectra normalized to the illumination source, respectively in red and blue for the island with R = 50 nm and with R = 80 nm. The insets in the graphs show the SEM top view images of the measured islands. Note that the noisy signal below 430 nm, in the top graph of Fig. 2(a), is due to the normalization to the illumination source. We compare the scattered signal with the FDTD normalized cross-sections of the two islands, reported in the bottom graphs in Fig. 2(a) and 2(b); the system is modelled as an island sitting atop 25 nm of SiO_2 separating it from the underlying Si bulk. We calculate the normalized scattering cross section (scattering cross section normalized to geometrical cross section calculated as the area of the bottom (bigger) circular surface of the island $\boldsymbol{\pi R}^2$) $Q_{sca}=\sigma_{scat}/\sigma_{geo}$ and modal field profiles inside the particles. Note that for now the pedestal is not introduced in simulations, in order to isolate the optical behaviour of the dewetted island sitting atop the substrate without the pedestal itself. The identification of Mie modes is performed by studying the field profiles inside the nanoparticle and identifying the corresponding current loops [8,21,34] :the crosscuts of the electric field intensity and current loops of the two islands extracted from the FDTD simulations are shown in Fig. 2(c) and (d). The wavelengths of acquisition of the crosscuts are highlighted with green dots in the spectra of Q_{sca}, and are respectively $\lambda = 450$ nm and $\lambda = 630$ nm in the case of R = 50 nm and R = 80 nm. We observe that the island of radius R = 80 nm exhibits a broad resonance centered around $\lambda \approx$ 550 nm both theoretically and experimentally. The crosscut of the electric field intensity, reported in Fig. 2(d) and characterized by a current vortex in the central part of the island, confirms that this resonance can be attributed to electric (ED) and magnetic dipole (MD), that are not distinguishable. The hybridization of the modes can be ascribed to the symmetry breaking with respect to the ideal case of a spherical Mie resonator in air. We label this band ED/MD resonance [8,21,34]. For the smaller island we found a slight mismatch between theory and experiment: numerical simulations predict that particles of radius smaller than 80 nm are too small to support Mie resonances in the studied spectral range [8,24]. This is confirmed by the analysis of Qsca of the smaller island (bottom Fig. 2(a)), and by the FDTD crosscut of the electric field intensity of Fig. 2(c) that clearly does not display any vortex.

However, the experimental spectrum displays a peak around $\lambda = 460$ nm, which is not revealed in simulations (see Q_{sca} in bottom graph of Fig. 2(a)). The same sharp and intense peak at about $\lambda = 460$ nm appears in the scattering spectrum of the island with radius 80 nm. Here and in the following, we will refer to this peak as $\boldsymbol{P}$. Also in this latter case, simulations are not able to catch this feature that is evident in the experimental spectra for wavelengths below 500 nm.

We complete the experimental analysis with the hyperspectral imaging provided by the SDOM technique (a sketch of the scanning process is shown in Fig. 3(a)). The reconstructed hyperspectral maps can be filtered around a single wavelength, or around a broad spectral interval. One pixel of the maps corresponds to a displacement of 200 nm. In Fig. 3(b) we report a dark-field map acquired on an array of islands of small dimension $R \approx 50$ nm. The map is filtered around the wavelength interval of [450-500] nm, which roughly corresponds to the spectral width of peak P. The map displays a localized scattering at these wavelengths in correspondence of each island. When considering the island with radius $R \approx 80$ nm (Fig. 3(c)) we showcase a zoomed map filtered around the same spectral window, [450-500] nm. Since for these nanoparticles a Mie resonance is present (ED/MD), we compare this map to that one filtered around ED/MD ($\lambda = [550\text{-}650]$ nm, Fig. 3(d)). From this comparison we see what has already been shown in [24], i.e., that in condition of tilted illumination the maximum collected signal can change position in the maps for different wavelengths.

We observe a shift of about 400 nm between the hotspot of the ED/MD resonance (Fig. 3(d)) and of peak P, while the collected intensity of P is unbalanced towards left in the map, ED/MD is more shifted to the right. This is a consequence of the tilted illumination [24].

To shed light on the physical origin of peak P, which also exhibits a strong spatial localization even for islands of smaller dimension, we refer to the morphological analysis (Fig. 1) which revealed the presence of a SiO_x pedestal under the dewetted nanoparticles. We address the problem in two phases: at first, to confirm the SiO_x chemical composition of the pedestal determined by interdiffusion mechanisms, a selective wet etching procedure is performed. Then, we perform a set of FDTD simulations in which the pedestal is modelled with different optical

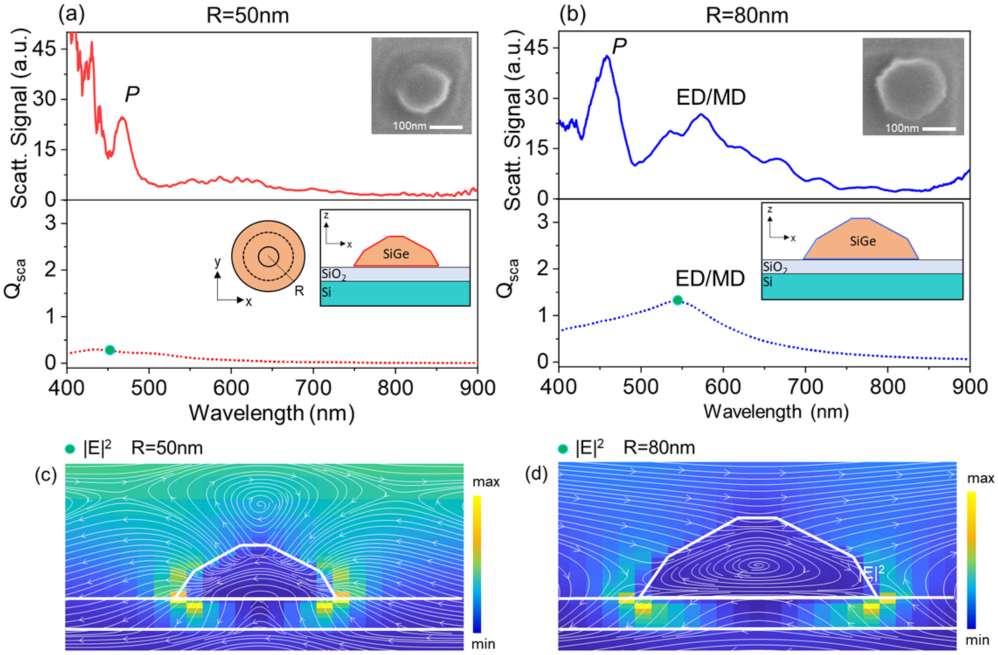

Fig. 2. a) and b) Upper graphs: Normalized dark-field spectrum of the islands of $R = 50$ nm and $R = 80$ nm. R is defined as the major radius corresponding to the bottom circular section of the island. The insets shows the top view SEM images of the investigated islands. Bottom graphs: FDTD Normalized scattering cross-sections Q_{sca} of the islands of $R = 50$ nm and $R = 80$ nm. The different indexes of refraction are highlighted in different colors in the sketch of the inset in the FDTD graphs. c) and d) FDTD Vertical crosscut of the electric field intensity and current loops (represented by white arrows) of the smaller and bigger nanoparticle acquired at $\lambda = 450$ nm and $\lambda = 550$ nm which are indicated in the Q_{sca} plots with a green dot.

constants taking into account the intermixing of Silicon and SiO_2. This second step helped us to establish a rough link between the chemical composition and scattering properties.

The selective wet etching procedure is carried out by using a 33% in volume KOH solution at 85°C. This wet-anisotropic etching, which is based on the selectivity of the alkaline solution, etches quickly silicon and very slowly the thermal SiO_2 and SiGe alloys [35,36]. The reproducibility of the wet process is validated by processing different samples batches, characterized in planar or tilted SEM view. In Fig. 4(a) it is shown a SEM top view of one of the dewetted islands together with its pedestal that will be used as a starting point for the selective etching process (t = 0s). After t = 8s of immersion at 85°C (Fig. 4(b)), the pedestal and the island don't show any significative variations. This effect immediately excludes a possible composition of the pedestal based on pure Si. However, the SiO_2 area close to the pedestal that has not been protected by the mask during the lithography EBL step and partially etched both by dry (RIE process) and both wet (DHF solution) etching treatments, presents the irregularities through which the KOH solution penetrates. The direct result is visible in Fig. 4(c), in which the contrast of the SEM image enhances the presence of the empty areas where the silicon has been selectively attacked respected the SiO_2 film. As the etching time increase to t = 25 s, in the cross-SEM image reported on Fig. 4(d) we observe that the SiGe island and the SiO_x pedestal are preserved, while the silicon bulk is etched, showing the typical inclination profile of 54.74° due to the anisotropic wet etching [37]. From this analysis we can therefore exclude that the pedestal is composed by pure Si.

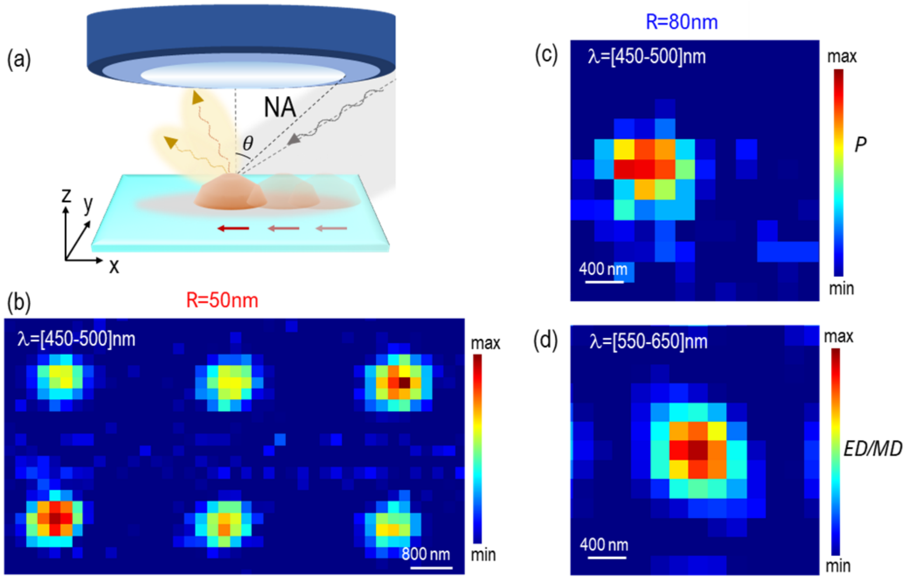

Fig. 3. a) Sketch of the SDOM setup. b) Dark-field hyperspectral map filtered around the wavelength interval [450-500]nm and obtained by scanning the pattern with islands of radius $R \approx 50$ nm. c) and d) Dark-field hyperspectral map of a single island of radius $R \approx 80$ nm filtered around two different spectral windows [450-500] nm and [550-650] nm

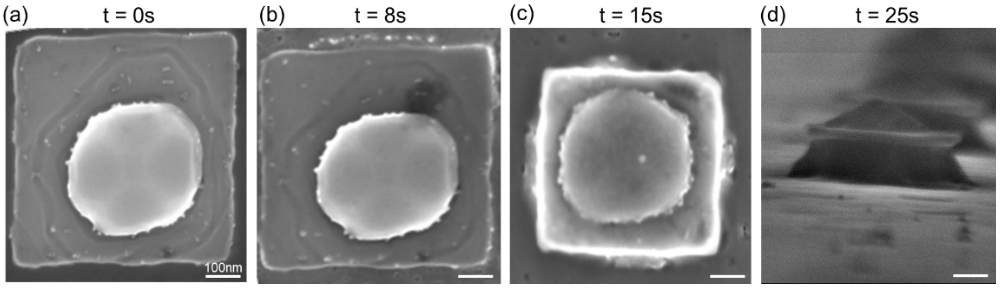

Fig. 4. SEM characterization of the different SiGe islands and their pedestal in TOP view before (a) the wet etching with KOH-based solution at 85°C, and after 8 sec (b and c) and after 25 sec (d). Figure (c) shows a detail of the SiO_2 material around the pedestal after 8 sec of wet etching. (d) Prospective view of the sample after 25 sec of etching. The scale bar in all SEM images is 100 nm.

We then proceeded to compare the optical spectra obtained with FDTD simulations assuming different rates of partial diffusion of silicon atoms in the SiO_2 pedestal [25,26]. Figure 5(a) shows the real part of silicon permittivity (blue line) as a function of wavelength along with its imaginary part (green line) and the permittivity of SiO_2 (red line). The blue curve shows a sharp peak centered around 430 nm, which we can correlate to the peak P ($\lambda = 460$ nm) found in the SDOM experiment. We therefore model in FDTD simulations the chemical composition of the pedestal through an “alloy”-type formula combining the permittivity of Si and SiO_2: in this way, the permittivity of the pedestal is $\varepsilon_P = a_P \varepsilon_{Si} + (1 - a_p)\varepsilon_{SiO_2}$ where $a_P = 0,\ 0.1 \ldots 1$ refers to the amount of Si in the pedestal. The same arguments, which hold for the SiO_2 layer between the Si bulk and the pedestal, is applied to calculate its permittivity $\varepsilon_L = a_L \varepsilon_{Si} + (1 - a_L)\varepsilon_{SiO_2}$,

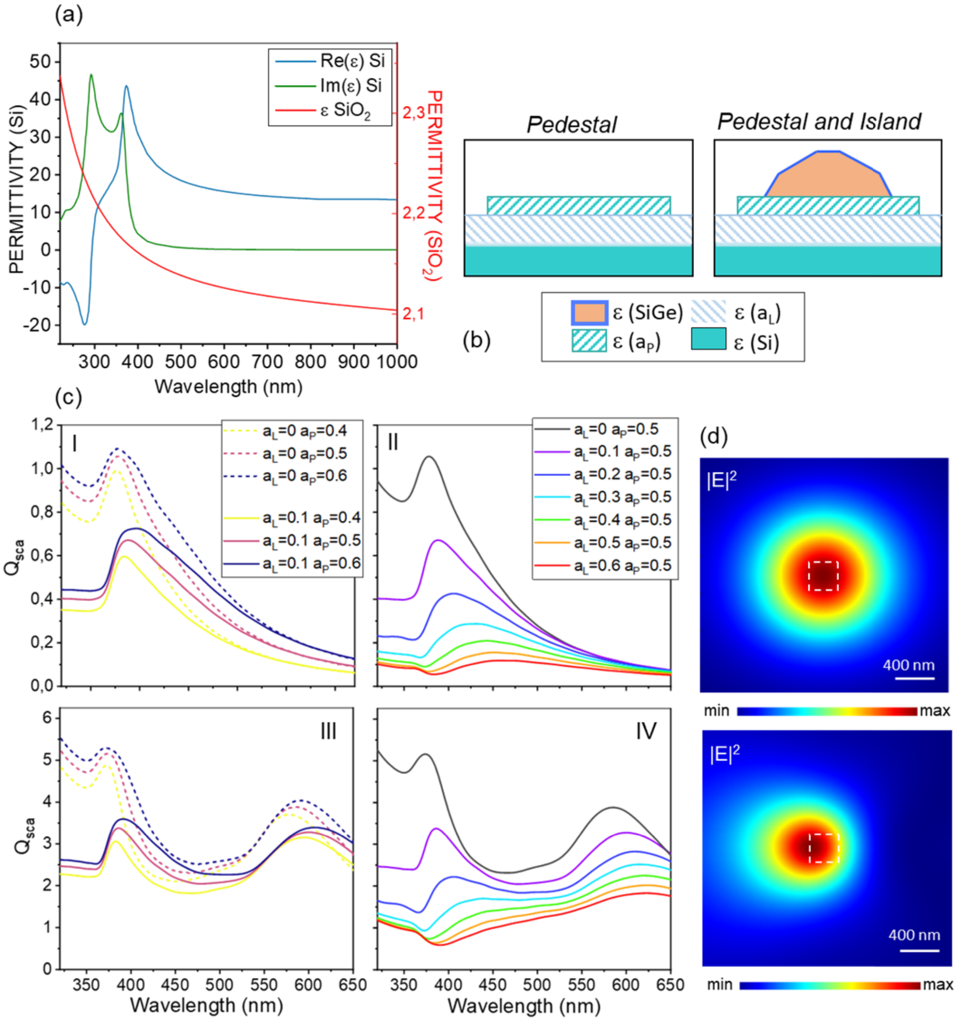

Fig. 5. (a) Real and imaginary parts of Silicon permittivity, compared with the SiO2 permittivity. (b) Sketches of the simulated models, respectively the pedestal and the island of R = 80 nm on top of the pedestal. The optical constants are highlighted in different colors following the labelling of the different optical constants. (c) Panels I and III: Q_{sca} of the pedestal and the island atop the pedestal plotted for $a_P = 0.4,\ 0.5,\ 0.6$ in absence of the contamination of Si in the layer ($a_L = 0$) (dashed lines), and for a fixed value of $a_L = 0.1$. Panels II and IV: Q_{sca} of the pedestal and the island atop the pedestal simulated for a fixed value of $a_P = 0.5$ and by varying $a_L = 0,\ 0.1 \ldots 0.6$. (d) FDTD electric field intensity maps of peak P and ED/MD calculated in the configuration $a_L = 0.1$ and of $a_P = 0.5$. The white dashed rectangle indicates the presence of the pedestal.

where $a_L = 0,\ 0.1 \ldots 1$ refers to the amount of Si in the layer. A sketch of the simulated models is reported in Fig. 5(b), along with the labelling of the different optical constants.

We therefore simulated a multilayer structure composed of the Si bulk, the intermediate 25 nm thick SiO_2 layer with the pedestal of permittivity $\varepsilon_P(a_P)$ on top.The results are calculated as a function of the Si contribution to the alloy of the pedestal (a_P). We do this to focus on the pedestal light scattering properties and to see if and how they are affected by the contribution of Silicon. In Fig. 5(c) (panel I), we compare the normalized scattering cross-sections Q_{sca} of pedestals (of area 325×325 nm^2 as those in the SEM image of Fig. 2(b), and 14 nm thick) for three different values of $a_P = 0.4,\ 0.5,\ 0.6$ (dashed lines). We observe that a scattering peak located around 380 nm is present. Moreover, by increasing the concentration of silicon, the peak scattering efficiency increases, and its spectral width broadens. As mentioned above, this scattering peak can be attributed to the refractive index of Si (see Fig. 5(a)).

We then add a minimum contribution of silicon also to the underlying layer (a_L=0.1) and calculate the normalized scattering cross-sections which are reported in panel I for $a_P = 0.4,\ 0.5,\ 0.6$ (solid lines in the same colorscale). We assume a nominal thickness of 25 nm for the layer: however, whenever the intermixing process occurs, it is not possible to know the exact value of its thickness. We note also that minimal variations of such thickness (±2-5 nm) have negligible effects on the optical response. Notably, considering the intermixing process also in the layer below the pedestal determines a redshift of the scattering peaks and a further spectral broadening which increases with a_P. Therefore, to selectively analyze the effect of the contribution of Si to the layer, we calculate the Q_{sca} of the pedestal for six values of $a_L = 0,\ 0.1 \ldots 0.6$ at a fixed value of $a_P = 0.5$. The results, shown in panel II of Fig. 5(c), clearly show that as a_L increases the peak redshifts but the scattering efficiency damps and for values larger than 0.4 the peak intensity is negligible. Hence it is possible to conclude that a minimum contribution of Si inside the layer must be taken into account to explain the experimental peak located around 450 nm, as it introduces a redshift in the scattering cross-section. However, this contribution is reasonably minimum, for example $a_L = 0.1 - 0.2$. In the configuration with $a_L = 0.1$ and $a_P = 0.5$, the scattering cross-section is in fairly good agreement with the dark-field spectrum of Fig. 2(a), acquired in the case of the smaller island, where no Mie resonance can be detected. In fact, the apparent spectral shift of about 70 nm between experiment and simulation (and the major sharpness of the dark-field peak), is explainable by taking into account the detection limit in our setup, which dramatically drops below 448 nm.

Finally, we simulate the dewetted SiGe island of $R = 80$ nm sitting atop the pedestal, and perform the simulations analogously with the previous ones: the normalized scattering cross-sections of the island are reported in panel III by varying only the contamination of the pedestal (dashed lines) and for a fixed value $a_L = 0.1$ (solid lines) for $a_P = 0.4,\ 0.5,\ 0.6$. We observe that the contribution of Si in the layer also induces a spectral redshift of the island's Mie resonance. The general picture is completed by calculating the scattering cross-sections of the island for the fixed value of $a_P = 0.5$, reported in panel IV for different values of $a_L = 0,\ 0.1 \ldots 0.6$. As also expectable from the results of panel I and II, by comparing the curves with the experimental spectrum of Fig. 2(b), we can conclude that the most reasonable configuration is $a_P = 0.5$ and $a_L = 0.1$, meaning a pedestal composed at 50% of Si and 50% of SiO_2, sitting atop a layer of SiO_2 with a 10% contamination of Si. This results are in agreement with what has been shown in previous works on the PL generated by SiOx layers where dimensional quantum confinement in silicon nanoclusters occurs and give rise to different emission bands in the visible and infrared region depending on the relative concentration [38]. In this configuration, we look at the FDTD spatial distribution of the electric field intensity for the two peaks P and ED/MD (see black spectrum in panel IV) generated under the illumination of a plane wave tilted by 30° with respect to the axis normal to the substrate; the maps are acquired with a monitor set at 1 μm distance from the island's surface, at the central wavelength of peak P and ED/MD, i.e. $\lambda = 450$ nm and $\lambda = 580$ nm. The white dashed square highlights the position of the pedestal. In the map of P we observe a circular distribution of the electric field intensity, whose hotspot is shifted towards left with respect to the one in the map of ED/MD. This is in a very good agreement with the dark-field maps of Fig. 3(c) and (d). The maps of Fig. 3(c) and (d) further confirm that the intensity lobes in the dark-field maps detected for both the island with $R = 50$ nm and $R = 80$ nm and filtered around peak P (λ=[460-500] nm) can be ascribed to the scattering properties of the pedestal, which scatters in the opposite direction of the illumination source.

4. Conclusions

In conclusion, we optically characterize a wide range of wavelengths, even lower than 500 nm not studied in detail so far. We demonstrate through simulations and by means of the SDOM technique that a SiO_x pedestal, deriving from the EBL process, is present under dewetted nanoparticles, and that it influences the scattering cross-section of the nanoparticle itself. The presence of a sharp peak at shorter wavelengths with respect to the Mie resonances range is explained by introducing a partial diffusion of silicon atoms in the pedestal and in the underlying silica layer. Through FDTD simulations, by tuning the optical permittivities with an alloy-type formula, we are able to clarify how the contamination of Si in the pedestal (and the underlying silica layer) affects the optical properties of the system and which percentage of Si is necessary to explain the experimentally detected peculiar optical feature. Notably, we showed how light scattered from the pedestal is strongly directed in the opposite direction of the illumination source. Our results might pave the way for novel exploitations of dewetted Mie resonator in light scattering directionality applications.

Funding. Consiglio Nazionale delle Ricerche (EPOCALE); European Research Council (828890); Ministero dell'Università e della Ricerca (PE 0000023 - NQSTI).

Disclosures. The authors declare no conflicts of interest.

Data availability. Data underlying the results presented in this paper are not publicly available at this time but may be obtained from the authors upon reasonable request.

References

1. A. I. Kuznetsov, A. E. Miroshnichenko, M. L. Brongersma, Y. S. Kivshar, and B. Luk'yanchuk, "Optically resonant dielectric nanostructures," Science **354**(6314), 20 (2016).
2. M. K. Schmidt, R. Esteban, J. J. Sáenz, I. Suárez-Lacalle, S. Mackowski, and J. Aizpurua, "Dielectric antennas - a suitable platform for controlling magnetic dipolar emission," Opt. Express **20**(13), 13636 (2012).
3. Y. Yang, I. I. Kravchenko, D. P. Briggs, and J. Valentine, "All-dielectric metasurface analogue of electromagnetically induced transparency," Nat. Commun. **5**(1), 5753 (2014).
4. A. Cordaro, J. van de Groep, S. Raza, E. F. Pecora, F. Priolo, and M. L. Brongersma, "Antireflection high-index metasurfaces combining Mie and Fabry-Pérot resonances," ACS Photonics **6**(2), 453–459 (2019).
5. T. Wood, M. Naffouti, J. Berthelot, T. David, J.-B. Claude, L. Métayer, A. Delobbe, L. Favre, A. Ronda, I. Berbezier, N. Bonod, and M. Abbarchi, "All-dielectric color filters using SiGe-Based Mie resonator arrays," ACS Photonics **4**(4), 873–883 (2017).
6. M. Kerker, D.-S. Wang, and C. L. Giles, "Electromagnetic scattering by magnetic spheres," J. Opt. Soc. Am. **73**(6), 765 (1983).
7. W. Liu and Y. S. Kivshar, "Generalized Kerker effects in nanophotonics and meta-optics [Invited]," Opt. Express **26**(10), 13085 (2018).
8. J. van de Groep and A. Polman, "Designing dielectric resonators on substrates: Combining magnetic and electric resonances," Opt. Express, **21**(22), 26285 (2013).
9. A. Pavel D, K. V. Terekhov, Y. A. Baryshnikova, A. K. Artemyev, A. S. Shalin, and A. B. Evlyukhin, "Multipolar response of nonspherical silicon nanoparticles in the visible and near-infrared spectral ranges," Phys. Rev. B **96**(3), 035443 (2017).
10. C. Pavel D, V. E. Terekhov, K. V. Babicheva, A. S. Baryshnikova, A. K. Shalin, and A. B. Evlyukhin, "Multipole analysis of dielectric metasurfaces composed of nonspherical nanoparticles and lattice invisibility effect," Phys. Rev. B **99**(4), 045424 (2019).
11. E. Pavel D, A. B. Terekhov, D. R. Evlyukhin, V. S. Volkov, A. S. Shalin, and A. Karabchevsky, "Magnetic octupole response of dielectric quadrumers," Laser Photonics Rev. **14**, 1900331 (2020).
12. Y. Meng, Y. Chen, L. Lu, Y. Ding, A. Cusano, J. A. Fan, Q. Hu, K. Wang, Z. Xie, Z. Liu, Y. Yang, Q. Liu, M. Gong, Q. Xiao, S. Sun, M. Zhang, X. Yuan, and X. Ni, "Optical meta-waveguides for integrated photonics and beyond," Light: Sci. Appl. **10**(1), 235 (2021).
13. K. I. Okhlopkov, A. Zilli, A. Tognazzi, D. Rocco, L. Fagiani, E. Mafakheri, M. Bollani, M. Finazzi, M. Celebrano, M. R. Shcherbakov, C. D. Angelis, and A. A. Fedyanin, "Tailoring third-harmonic diffraction efficiency by hybrid modes in High-Q metasurfaces," Nano Lett. **21**(24), 10438–10445 (2021).

14. B. S. Krasikov, M. Odit, D. Dobrykh, I. Yusupov, A. Mikhailovskaya, D. Shakirova, A. Shcherbakov, A. Slobozhanyuk, P. Ginzburg, D. Filonov, and A. Bogdanov, "Multipolar Engineering of subwavelength dielectric particles for scattering enhancement," Phys. Rev. Appl. **15**(2), 024052 (2021).
15. M. Abbarchi, M. Naffouti, M. Lodari, M. Salvalaglio, R. Backofen, T. Bottein, A. Voigt, T. David, J.-B. Claude, M. Bouabdellaoui, A. Benkouider, I. Fraj, L. Favre, A. Ronda, I. Berbezier, D. Grosso, and M. Bollani, "Solid-state dewetting of single-crystal silicon on insulator: effect of annealing temperature and patch size," Microelectron. Eng. **190**, 1–6 (2018).
16. M. Abbarchi, M. Naffouti, B. Vial, A. Benkouider, L. Lermusiaux, L. Favre, A. Ronda, S. Bidault, I. Berbezier, and N. Bonod, "Wafer scale formation of monocrystalline silicon-based Mie resonators via silicon-on-insulator dewetting," ACS Nano **8**(11), 11181–11190 (2014).
17. M. Bollani, M. Salvalaglio, A. Benali, M. Bouabdellaoui, M. Naffouti, M. Lodari, S. D. Corato, A. Fedorov, A. Voigt, I. Fraj, L. Favre, J. B. Claude, D. Grosso, G. Nicotra, A. Mio, A. Ronda, I. Berbezier, and M. Abbarchi, "Templated dewetting of single-crystal sub-millimeter-long nanowires and on-chip silicon circuits," Nat. Commun. **10**(1), 5632 (2019).
18. M. Salvalaglio, M. Bouabdellaoui, M. Bollani, A. Benali, L. Favre, J.-B. Claude, J. Wenger, P. de Anna, F. Intonti, A. Voigt, and M. Abbarchi, "Hyperuniform monocrystalline structures by spinodal solid-state dewetting," Phys. Rev. Lett. **125**(12), 126101 (2020).
19. A. Benali, J.-B. Claude, N. Granchi, S. Checcucci, M. Bouabdellaoui, M. Zazoui, M. Bollani, M. Salvalaglio, J. Wenger, L. Favre, D. Grosso, A. Ronda, I. Berbezier, M. Gurioli, and M. Abbarchi, "Flexible photonic devices based on dielectric antennas," JPhys Photonics **2**(1), 015002 (2020).
20. M. Naffouti, R. Backofen, M. Salvalaglio, T. Bottein, M. Lodari, A. Voigt, T. David, A. Benkouider, I. Fraj, L. Favre, A. Ronda, I. Berbezier, D. Grosso, M. Abbarchi, and M. Bollani, "Complex dewetting scenarios of ultrathin silicon films for large-scale nanoarchitectures," Sci. Adv. **3**(11), eaao1472 (2017).
21. N. Granchi, M. Montanari, A. Ristori, M. Khoury, M. Bouabdellaoui, C. Barri, L. Fagiani, M. Gurioli, M. Bollani, M. Abbarchi, and F. Intonti, "Near-field hyper-spectral imaging of resonant Mie modes in a dielectric island," APL Photonics **6**(12), 126102 (2021).
22. L. Fagiani, N. Granchi, A. Zilli, C. Barri, F. Rusconi, M. Montanari, E. Mafakheri, M. Celebrano, M. Bouabdellaoui, M. Abbarchi, F. Intonti, A. Khursheed, P. Biagioni, M. Finazzi, M. A. Vincenti, and M. Bollani, "Linear and nonlinear optical properties of dewetted SiGe islands," Opt. Mater.: X **13**, 100116 (2022).
23. D. Toliopoulos, M. Khoury, M. Bouabdellaoui, N. Granchi, J.-B. Claude, A. Benali, I. Berbezier, D. Hannani, A. Ronda, J. Wenger, M. Bollani, M. Gurioli, S. Sanguinetti, F. Intonti, and M. Abbarchi, "Fabrication of spectrally sharp Si-based dielectric resonators: combining etaloning with Mie resonances," Opt. Express **28**(25), 37734 (2020).
24. N. Granchi, L. Fagiani, M. Salvalaglio, C. Barri, A. Ristori, M. Montanari, M. Gurioli, M. Abbarchi, A. Voigt, M. A. Vincenti, F. Intonti, and M. Bollani, "Engineering and detection of light scattering directionalities in dewetted nanoresonators through dark-field scanning microscopy," Opt. Express **31**(5), 9007 (2023).
25. F. Leroy, Y. Saito, S. Curiotto, F. Cheynis, O. Pierre-Louis, and P. Müller, "Shape transition in nano-pits after solid-phase etching of SiO_2 by Si islands," Appl. Phys. Lett. **106**(19), 191601 (2015).
26. F. Leroy, D. Landru, F. Cheynis, O. Kononchuk, P. Müller, and S. Curiotto, "Kinetics and coupled dynamics of dewetting and chemical reaction in $Si/SiO_2/Si$ system," J. Mater. Sci. **55**(34), 16074–16082 (2020).
27. V. Mondiali, M. Lodari, M. Borriello, D. Chrastina, and M. Bollani, "Top–down SiGe nanostructures on Ge membranes realized by e-beam lithography and wet etching," Microelectron. Eng. **153**, 88–91 (2016).
28. M. Bollani, D. Chrastina, A. Fedorov, R. Sordan, A. Picco, and E. Bonera, "Ge-rich islands grown on patterned Si substrates by low-energy plasma-enhanced chemical vapour deposition," Nanotechnology **21**(47), 475302 (2010).
29. M. Brehm, H. Lichtenberger, T. Fromherz, and G. Springholz, "Ultra-steep side facets in multi-faceted SiGe/Si(001) Stranski-Krastanow islands," Nanoscale Res. Lett. **6**(1), 70 (2011).
30. L. inc., https://www.lumerical.com/products/fdtd/.
31. D. E. Aspnes and A. A. Studna, "Dielectric functions and optical parameters of Si, Ge, GaP, GaAs, GaSb, InP, InAs, and InSb from 1.5 to 6.0 eV," Phys. Rev. B **27**(2), 985–1009 (1983).
32. G. E. Jellison, T. E. Haynes, and H. H. Burke, "Optical functions of silicon-germanium alloys determined using spectroscopic ellipsometry," Opt. Mater. **2**(2), 105–117 (1993).
33. I. H. Malitson, "Interspecimen comparison of the refractive index of fused silica," J. Opt. Soc. Am. **55**(10), 1205 (1965).
34. J. Berzinš, S. Indrišiūnas, K. van Erve, A. Nagarajan, S. Fasold, M. Steinert, G. Gerini, P. Gečys, T. Pertsch, S. M. B. Bäumer, and F. Setzpfandt, "Direct and high-throughput fabrication of Mie-resonant metasurfaces via single-pulse laser interference," ACS Nano **14**(5), 6138–6149 (2020).
35. V. Mondiali, M. Lodari, D. Chrastina, M. Barget, E. Bonera, and M. Bollani, "Micro and nanofabrication of SiGe/Ge bridges and membranes by wet-anisotropic etching," Microelectron. Eng. **141**, 256–260 (2015).
36. N. A. Baidakova, V. A. Verbus, E. E. Morozova, A. V. Novikov, E. V. Skorohodov, M. V. Shaleev, D. V. Yurasov, A. Hombe, Y. Kurokawa, and N. Usami, "Selective etching of Si, SiGe, Ge and its usage for increasing the efficiency of silicon solar cells," Semiconductors **51**(12), 1542–1546 (2017).
37. H. Seidel, L. Csepregi, A. Heuberger, and H. Baumgärtel, "Anisotropic etching of crystalline silicon in alkaline solutions: I . Orientation dependence and behavior of passivation layers," J. Electrochem. Soc. **137**(11), 3612–3626 (1990).

38. Z. J. Hernández Simón, J. A. L. López, A. D. H. de la Luz, S. A. Pérez García, A. B. Lara, G. García Salgado, J. Carillo López, G. O. Mendoza Conde, and H. P. Martínez Hernández, "Spectroscopic Properties of Si-nc in SiOx Films Using HFCVD," Nanomaterials **10**(7), 1415 (2020).